

## 5. Calibration of *FIRAS* Data

In the initial part of the calibration processing, calibration data and sky data are treated essentially identically. The coadded IFGs are apodized and padded, and then Fourier transformed to produce complex-valued spectra. The spectra are converted from counts to volts at the detector upon division by the analog-to-digital converter scale factor and by the electronics transfer function. The processing of the calibration data and the sky data then diverges. The calibration coadds (and their associated covariance matrices) are used as input to the calibration model program (FISH) to derive a solution, and both the calibration and the sky coadds are calibrated with the resulting solution. The initial apodization and padding of the calibration data are done by the FFL facility; the final apodization, padding and calibration for both the calibration and sky data is done by the FSL facility.

### 5.1. Apodization and Padding

The coadded interferograms (IFGs) are apodized before Fourier transformation into spectra. The apodization function  $A(x)$  is an asymmetric smooth window function which enhances the signal-to-noise ratio for wide spectral features and reduces ringing from spectral lines.  $A(x)$  is designed to have a value of one at the IFG peak, to correctly weight the long and short sides of the IFG, and to fall off smoothly to zero at the ends.

The piecewise expression for the apodization function  $A(x_i)$  for the 512 sampled data points in the IFGs is:

$$A_i = f_i \left[ 1 - \left( \frac{i - c}{j - c} \right)^4 \right]^2 \quad (5)$$

where  $i \in [1, 512]$  is the IFG sample number,  $c$  is the IFG peak position given in Table 5.1. For the low spectral resolution data  $j = 1$  and

$$f_i = \begin{cases} 0 & i \in [1, 2] \\ 2 & i \in [3, 2c - 513] \\ \left\{ 3 - \cos \left( \frac{\pi(2c-482-i)}{30} \right) \right\} / 2 & i \in [2c - 512, 2c - 483] \\ 1 & i \in [2c - 482, 482] \\ \left\{ 1 - \cos \left( \frac{\pi(513-i)}{30} \right) \right\} / 2 & i \in [483, 512] \end{cases} \quad (6)$$

For the high spectral resolution data  $j = 513$  and

$$f_i = \left\{ \begin{array}{ll} 0 & i \in [1, 2] \\ \left\{ 1 - \cos \left( \frac{\pi(i-2)}{30} \right) \right\} / 2 & i \in [3, 32] \\ 1 & i \in [33, 2c - 32] \\ \left\{ 3 - \cos \left( \frac{\pi(i+32-2c)}{30} \right) \right\} / 2 & i \in [2c - 31, 2c - 2] \\ 2 & i \in [2c - 1, 512] \end{array} \right\} \quad (7)$$

The Fourier transform of  $A(x)$  gives the instrumental spectral window function before the calibration gain correction is applied and is the dominant factor in determining the instrument line profile and the frequency-to-frequency noise correlation. The full width half maximum of the Fourier transform of  $A(x)$  is  $0.8191 \text{ cm}^{-1}$  (24.56 GHz) for the low resolution spectra and  $0.2331 \text{ cm}^{-1}$  (6.988 GHz) for the high resolution spectra. See Figure 5.1 for the low and high resolution apodization functions.

Table 5.1: *FIRAS* IFG Peak Positions

Channel and Scan Mode	Peak Position Sample	Resolution ( $\text{cm}^{-1}$ )
LHSS RHSS	357	0.8191
LHSF RHSF	359	0.8191
LHLF RHLF	355	0.8191
LLSS RLSS	360	0.8191
LLFS RLFS	90	0.8191
LLFL RLFL	90	0.8191
LLLF RLLF	90	0.2331

In the *FIRAS* instrument the zero path difference is at bin  $\sim 355$ , so there are 355 independent frequencies available. There are only 512 points, so 256 complex points in the transform provide a complete description. Ideally, the response of the instrument is symmetric with respect to the zero path difference position of the MTM. Therefore, the antisymmetric part of the IFG is an indication of model errors, instrument imperfections, and unresolved spectral features. The antisymmetric part of the IFG is transformed to the imaginary part of the spectrum. The short side of the interferogram is padded by appending zeros. This padding is asymmetric, so the loss of degrees of freedom is concentrated in the imaginary part as well. The information about the sky is concentrated in the real part of the spectrum, but the imaginary part still has information relevant to

the instrument performance. Therefore, the full spectra are calibrated but only the real part is subsequently analyzed.

If the imaginary part of the spectrum is ignored, only the real part of the covariance matrix need be considered. Padding the interferogram beyond 710 ( $2 \times 355$ ) points forces the real part of the matrix to become singular. The process is not abrupt: as the padding is extended the condition number of the covariance matrix rises until numerical problems in finding the inverse actually obscure the point of formal singularity. We chose to pad the 512 point interferograms with 128 zeros as a compromise between getting all of the sky information in the real part of the spectrum and retaining a well-behaved covariance matrix. This results in 320 spectral points, allowing a direct comparison to previous results in 1/5 of the new points (1/4 of the previous points). The full covariance matrix is singular, but the covariance matrix of the real part of the spectrum is easily inverted.

The complex spectra are retained until after the calibration so that all of the instrumental effects can be modeled and removed. The uncertainties used in the calibration modeling use only the diagonal parts of the covariance matrix.

## 5.2. Channel Specific Items

Nominally each detector-scan mode combination is calibrated separately. There are two path lengths and two speeds of the MTM, resulting in four possible modes of operation (SF, SS, LF, and LS). There are four detectors (LH, LL, RH, RL) for 16 separate calibrations. However, the LS mode was used for only a few days in orbit, so there was little point in trying to use these data. About half of the data were in SS mode and this mode has the best calibration data. The LF mode for the low frequencies has high resolution. However, the Nyquist frequency is  $36 \text{ cm}^{-1}$ , so for the high frequencies (LH and RH) the LF data are truncated on board the *COBE* spacecraft rather than averaged; thus, their format is like that of the SF data.

The high frequency LF data look like the high frequency SF data with two important differences. First, the SF IFGs are averages of 16 sweeps of the MTM while the LF data are averages of only four sweeps, so each SF IFG receives approximately four times the weight of an LF IFG in both the calibration and the sky data. Second, differing numbers of A→D conversions are discarded for the LF and SF data, so that there is a 3.5 bin offset between the two data sets. An offset of three bins is removed by simple rotation, and the extra half bin of offset is removed by a phase adjustment after the Fourier transform is applied. Thus, the LHSF and LHLF data sets are combined into a single LHFA data set

and the RHSF and RHLF data sets are combined into RHFA.

Only the low frequency LF mode has the higher resolution; to preserve it, there are two separate calibrations performed on the low LF data. The first calibrates the LF data with high resolution, while the second combines the SF and LF data. To calibrate the SF data, each coadd is added in groups of four to mimic the processing done on the LF data on board the *COBE* spacecraft. This reduces the Nyquist frequency to  $36 \text{ cm}^{-1}$  and the length of the coadd to 128. These “decimated” SF coadds are given the scan mode FS. The LF coadds are then truncated to 128 points which reduces the resolution to that of the other data; these are given the scan mode FL. The apodization and padding for the combined low FS and FL coadds must also be reduced by a factor of four. This is accomplished by averaging the apodization function in groups of four (Section 4.4). The LLFS and LLFL data are combined into LLFA, and the RLFS and RLFL into RLFA.

Thus there are 10 separate calibrations: LHSS, LHFA, RHSS, RHFA, LLSS, LLLF, LLFA, RLSS, RLLF and RLFA. The LL detector performed much better than the RL detector and the RH detector performed much better than the LH detector. Since most of the calibration was done in SS mode, the LLSS and RHSS provide much of the information. However, the other modes provide additional information and instrument checks. The high resolution  $x\text{LLF}$  ( $x \in [L, R]$ ) and low resolution  $x\text{LFA}$  are not independent, as both include a portion of the  $x\text{LLF}$  data, (‘a portion’ because the  $x\text{LFA}$  data are truncated).

### 5.3. Instrument Calibration

Each calibration model consists of several thousand parameters (the exact number depends on the channel). The parameters are grouped into a set of about 20 parameters describing the bolometers and general instrument; a set of  $12 \times n$  emissivities, where  $n$  is the number of frequencies; and a set of  $5 \times m$  temperatures, where  $m$  is the number of coadds in the calibration. The parameters are adjusted by a simultaneous least squares fit to the calibration coadds in the program FISH. The calibration model is summarized here and discussed in Appendix C. Each set of parameters is uncertain, and the uncertainties can be propagated to the final sky spectra using the Jacobian ( $\partial S/\partial p$ ). The uncertainties for the different sets are given separate names for convenience: *JCJ*, for the bolometer and general parameters;  $P_0EP_0$ , for the emissivities; and *PUP*, for the temperature parameters (Section 7). The *FIRAS* calibration model is composed of a nine-parameter model of the bolometer response function and a linear photometric model of the instrument throughput.

### 5.3.1. Electronics Transfer Function

The first step in the calibration process is to undo the electronics to get the potential at the bolometer rather than at the A→D converter. The electronics transfer function (ETF) is an analytic model of the instrument’s post-detector analog and digital filters, including a 6-pole DC-blocking filter, a 5-pole Bessel filter, a treble boost, a digital lowpass filter, and smoothing due to data compression. This is included mainly as a convenience. Any errors in the ETF are compensated for by the optical transfer function (Section 5.3.3). Figure 5.1 gives the electronics transfer functions for LLSS, RHSS, and LLLF. The ETFs for the other channels are similar.

### 5.3.2. Bolometer Parameters

The bolometer resistance is modeled as:

$$R(T, E) = R_o \exp(T_o/T)^{1/2}(x/\sinh(x)) \quad x = E\rho/T, \quad (8)$$

where  $R_o$  gives the detector resistance at infinite temperature,  $T_o$  is a characteristic temperature,  $T$  is the temperature of the bolometer,  $x$  is a dimensionless variable,  $E$  is the electrical potential across the detector, and  $\rho$  is a constant involving the electron charge, characteristic hopping length, and length of the detector. The bolometer temperature is a balance between the radiation heating it and the conduction to the housing cooling it. The cooling power is modeled by  $P = G(T^{\beta+1} - T_c^{\beta+1})$  where  $G$  is a constant describing the geometry of the detector mounting and  $\beta$  is the index of thermal conduction for the material. The heat capacity of the bolometer is modeled as  $H = C_1T + C_3T^3$  (Mather 1982, 1984a, 1984b). Although the parameters ( $R_o, T_o, G, \beta, \rho, C_1, C_3$ ) were measured for each bolometer before launch the calibrations refit  $R_o, G, \rho, C_1$  with the orbital data. There is not enough temperature variation in the orbital data to fit  $T_o$  and  $\beta$  or to simultaneously fit  $C_1$  and  $C_3$ .

The bolometers were closely coupled to a JFET acting as an amplifier inside the dewar. The offset  $J_o$  and gain  $J_g$  of the JFET are also parameters of the model. The offset was fit along with everything else, but the gain was determined an analysis of the temporal response in the data immediately after a change in the bias voltage, using in orbit data

The bolometer model uses the linear small-signal approximation of the non-linear bolometer model to compute the bolometer’s operating temperature, time constant, and DC responsivity from its bath temperature, commanded bias, and readout voltage. The bolometer response function,  $B$ , is computed from the detector’s time constant ( $\tau$ ) and DC

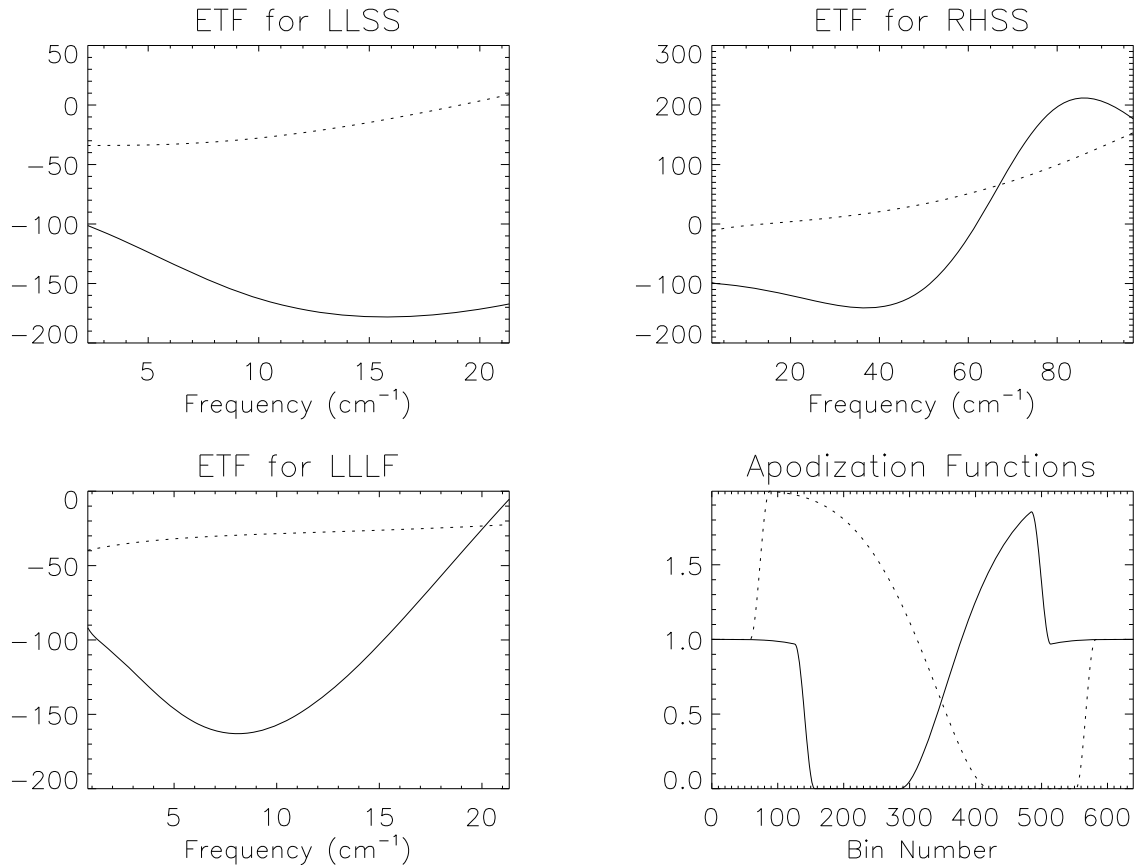


Fig. 5.1.— Electronics transfer functions for LLSS, RHSS and LLLF and apodization functions for low and high resolution data — For each of the ETF plots, the solid line is the real part and the dotted line is the imaginary part. For the apodization functions, the solid line is the low resolution (RHSS; the other low resolution apodization functions are nearly the same), and the dotted is the high resolution (LLLF and RLLF).

---

responsivity ( $S_o$ ):

$$B(\omega) = \frac{S_o}{1 + i\omega\tau} \quad (9)$$

at audio frequency  $\omega$ .

There are another ten parameters to model certain faults in the instrument. Three of these model a drift in the ICAL thermometry  $T' = T + A \exp(t/\tau_{ICAL}) + T_{\text{offset}}$ .  $T$  is the “raw” ICAL temperature, which is converted to  $T'$  by adding  $T_{\text{offset}} = -3.054$  mK and an exponential decay with amplitude  $A = 4.26$  mK and time constant  $\tau_{ICAL} = 104.3$  days. The parameters were chosen after many fits on all of the detectors. It is not entirely clear that the problem was in the ICAL or its thermometers, but the fact that it was seen in all detectors and scan modes and in both the sky and calibration data indicates that it is truly an optical drift. All of the channels used the same parameters to preserve the comparison used in destriping.

Analysis indicates that a reflectance of  $\sim 4\%$  as seen in the ICAL can lead to significant second and third harmonic response in the instrument. Hence two parameters were included to model this effect. These might be different for different detectors so they were fit along with the other parameters.

Finally, vibrations of the MTM at 57.57 and 8.32 Hz were detected, which led to ghost spectra around the vibration lines. These were modeled with a time varying amplitude determined by either a constant or a fourth order polynomial, depending on the channel and vibration frequency.

The derivative of the model was found with respect to each of these parameters both for use in the FISH program and to model the uncertainties due to the errors in estimating these parameters. These are combined and orthogonalized to form the *JCJ* uncertainties, which are discussed in Section 7.3.

### 5.3.3. Emissivities

The full optical model includes seven frequency-dependent emissions from the external calibrator, the internal calibrator, the sky horn, the reference horn, the dihedral mirrors, the structure, and the bolometers. Each of these is complex, but the total at each frequency is constrained to be zero by the Kirchoff condition. So, there are 12 free parameters at each frequency. Since the external calibrator is assumed to be good, its emission is identified as the transfer function, and the emissivities of the other elements are the ratio of their emission to the external emission. Uncertainties in these emissivities

propagate to the sky in the  $P_0EP_0$  uncertainty (Section 7.2).

The amplitudes of the emissions are shown in Figure 5.2; for the phases see Section 7.9.1. The ripples in the transfer function at low frequencies are due to channel reflection from the front and back of the filter. The deep trough at  $\sim 20 \text{ cm}^{-1}$  occurs because the low filter turns off before the reflected (high) signal turns on. Ripples at  $\sim 55$  and  $\sim 67 \text{ cm}^{-1}$  are due to an interference effect between the polarizers. These also appear in the ICAL emissivity.

The horns are well matched at low frequencies but diverge beyond  $30 \text{ cm}^{-1}$ . The sky horn is much larger than the reference horn: only the length to diameter is matched. The bolometer is kept at  $\sim 1.5 \text{ K}$ , so its radiation is essentially zero for  $\nu > 10$ . Similarly, the dihedral radiation is essentially zero for  $\nu > 30$ , as its temperature is less than  $5.5 \text{ K}$ . The high frequency bolometer and dihedral emissivities allow mismatch in the other emissivities (*i.e.* stray light) to be accommodated.

#### 5.3.4. Temperature and Phase Corrections

Although the temperatures of all of the important components of the *FIRAS* were measured with a precision of approximately  $1 \text{ mK}$ , the photometric precision is better than this. The temperatures of the four controllables (XCAL, ICAL, sky horn, and reference horn) were accordingly adjusted to best fit the photometry along with all of the other parameters. These adjustments were constrained with an estimate of the precision of the temperature measurement. The errors are typically a fraction of  $1 \text{ mK}$ . Although temperature errors propagate to the other parameters in the calibration model, they do not directly propagate to the sky data, as the temperature measurements of the *FIRAS* during the calibration are not used in the sky calibration. The temperature measurements taken during the sky observations are used, however, and these do propagate to the sky data. These are called the *PUP* uncertainty (Section 7.4).

The phase of the interferograms varied by a significant amount. Some of the variation was identified as due to the amplifier having different delay for different gains, but this did not explain the entire effect. Instead a phase was fit, with constraint, for each coadd. This method was also used on the sky data. These phases are included with the temperature adjustments, as they have the same size and same correlations as the other uncertainties (Figure 5.3).

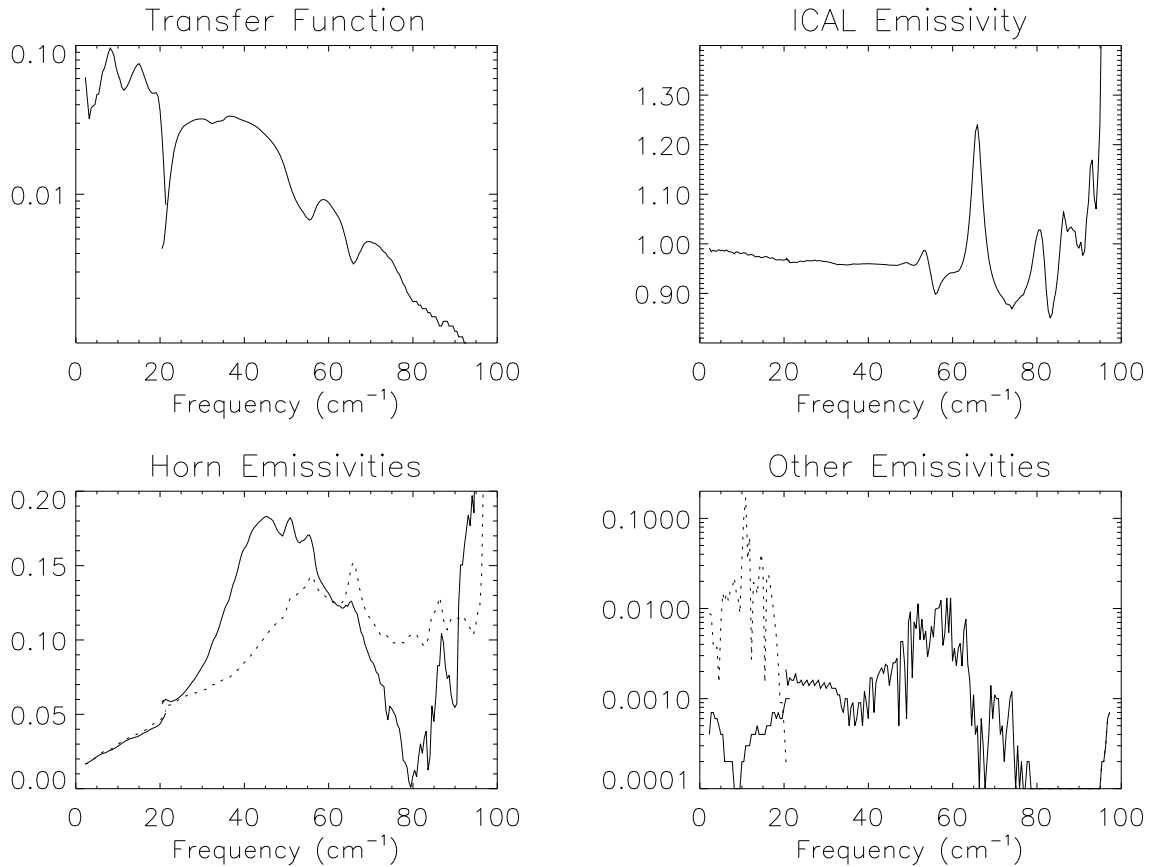


Fig. 5.2.— Optical transfer function and emissivities — The values for LLSS (2–21 cm<sup>-1</sup>) and RHSS (20–97 cm<sup>-1</sup>) are shown here. (a) Transfer function (logarithmic scale). (b) ICAL emissivity. (c) The sky (solid curve) and reference horn (dotted curve) emissivities. (d) Dihedral (solid) and bolometer (dotted) emissivities; the bolometer emissivity is only relevant for low frequencies. See text for discussion.

---

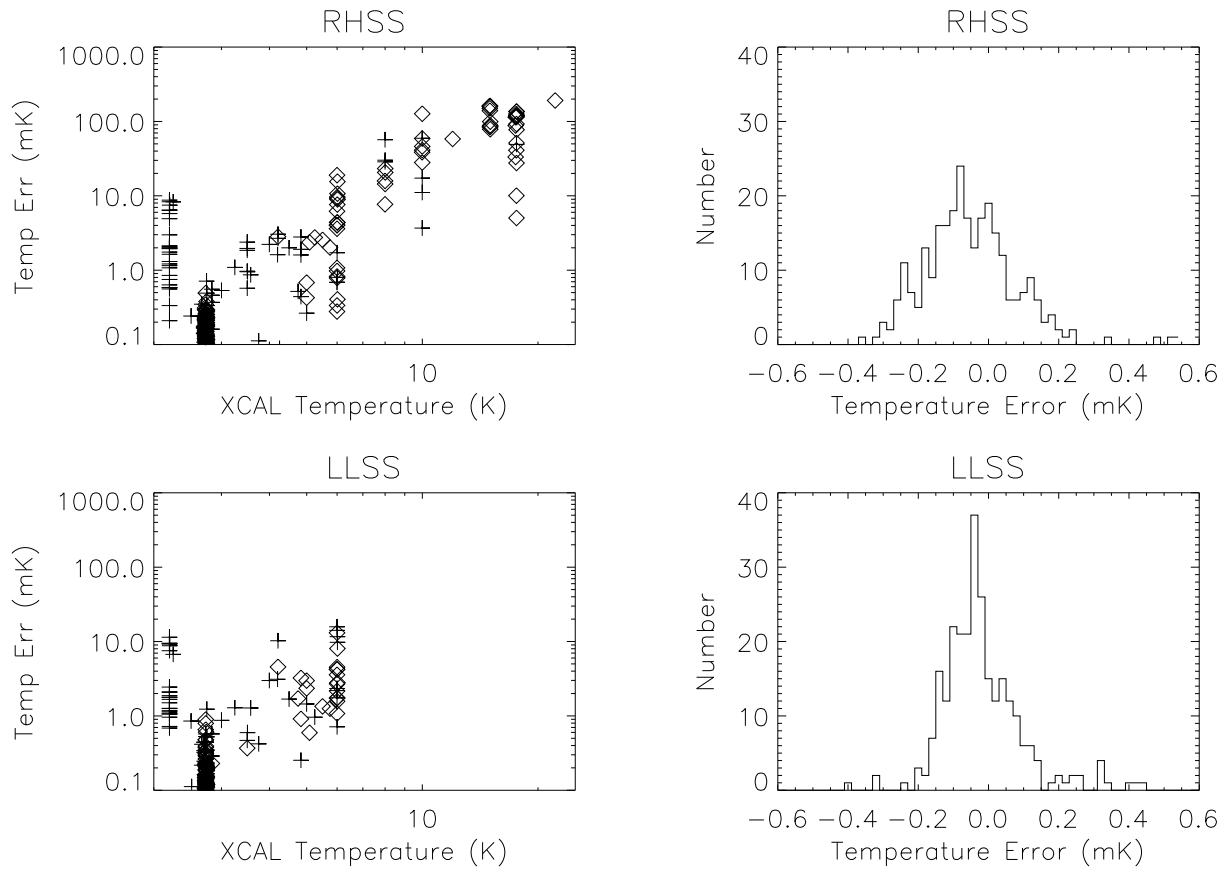


Fig. 5.3.— Photometric XCAL temperature adjustments — The values for RHSS (top plots) and LLSS (bottom plots) calibrations are shown here. The left hand plots are the adjustments (in mK), plotted as a function of XCAL temperature (in K). The symbol + indicates a positive correction, and the symbol  $\diamond$  indicates a negative correction. Temperatures greater than 7K are not used in LLSS. On the right are histograms of temperature adjustments for cold nulls (i.e. all controllables  $\sim 2.7$ K).

---

## 5.4. Temperature Scale Calibration

To first order the errors in the temperatures other than the XCAL are removed by the calibration process, as the same errors are repeated in the sky measurements. This section covers the XCAL thermometry calibration.

### 5.4.1. Frequency Scale Calibration

The frequency scale calibration of the *FIRAS* was determined from observations of the interstellar emission lines. Analysis of the [C II] and [N II] lines in the high frequency spectra, using the line profiles described in Section 8.4, shows that the frequency calibration is self-consistent to 0.005% at  $60\text{ cm}^{-1}$  (1800 GHz). Analysis of the CO lines in the low frequency spectra has shown that the frequency calibration is self-consistent to 0.03% at  $15\text{ cm}^{-1}$  (450 GHz). It is possible that there may be non-linear variations in the frequency scale due to beam divergence within the instrument. Thus, even though the [C II] and [N II] lines have better resolution the low frequency scale was used to determine the CMBR cosmic parameters. The frequency scale is set by the CO and [C I] lines observed in that data.

### 5.4.2. Temperature Calibration

Twenty-four germanium resistance thermometers (GRTs) are mounted throughout the *FIRAS* to measure the temperatures of various components of the instrument. These GRTs were calibrated before flight relative to a NIST-calibrated standard GRT, nominally to 1 mK accuracy. Eight calibration resistors are used to convert the GRT readings from counts to ohms. Readings from the 24 GRTs are combined to yield temperatures of ten components of the instrument: the external and internal calibrators, the sky and reference horns, the four detectors, the mirrors on the mirror transport mechanism, and the instrument structure. The weights for the combination of GRT readings are discussed in Section 9.1.

The temperature scale of the *FIRAS* was calibrated in two ways. In the first method, temperature readings from three GRTs attached to different locations on the external calibrator were averaged to produce a measured temperature of the calibrator. In the second method the calibration model included an additive correction to the measured temperature of the external calibrator. This parameter resulted in a determination of the color temperature scale of the XCAL, which ties the calibrated frequency scale to

temperatures through the form of the Planck function. This analysis gives an estimated adjustment to the *FIRAS* thermometer scale of  $-4.5 \pm 1.0$  mK. We split the difference to make a 2.25 mK temperature correction (Section 7.5) and claim a systematic precision of 2 mK (one  $\sigma$ ).

### 5.5. Calibration Performance

The validity of the  $\chi^2$  calculations depend on the variance that the calibration program assigns to the input data. Determining this for the low temperature null data (*i.e.* those data taken with all four controllables at  $\sim 2.7$ K) is straightforward. There are  $\sim 18000$  IFG's taken in this state, so the observed measurement variation determines the variance to  $\sim 1\%$ . For other temperature combinations there are only a few tens of IFG's in each combination, so the variance using just a particular temperature condition's data can only be determined to  $\sim 10\text{--}20\%$ . For higher temperatures the thermometers don't read as precisely, and the temperature variations (which are fit in the calibration program) can artificially inflate the uncertainty estimates. Also, the gain is turned down, so the true noise can be hidden within a single bit.

To estimate the variance of the higher temperature data, all of the data are used to fit a phenomenological model for the data variance:

$$\sigma_\nu(T) = D_\nu(T_x^2 + T_i^2 + 0.1T_s^2 + 0.1T_r^2)/(2.2 \cdot 2.7^2) \quad (10)$$

which gives approximately the right scale to the variance in the input data. However, the  $\chi^2$  for the high temperature data is still high (Table 5.2 and Figure 5.4), particularly for the high frequency data.

Table 5.2 shows the  $\chi^2$  per degree of freedom. The “Null” column is for the cold null data, where all controllables are  $\sim 2.7$ K. The “Hot” column is for the data where at least one element is greater than 2.8K. In addition, there are  $\chi^2$  and degree of freedom errors introduced when determining the temperature adjustments phase, bolometer parameters, *etc.*, which account for the discrepancy between the “Detector”  $\chi^2$  and the “Final”  $\chi^2$ .

For the low frequency calibrations we exclude all of the data with any of the controllable temperatures above 7K. This reduces the requirements on the calibration model, as the detector radiation loading scales approximately as  $T^4$ , and the total power is a key issue in the detector model. For the high frequency detectors we must include the data with temperatures up to 22K in order to get sufficient power at  $95 \text{ cm}^{-1}$  to calibrate the instrument. This leads to distortions in the high frequency detector calibration models, so they are not as precise as the low frequency models.

Table 5.2:  $\chi^2$  per Degree of Freedom

Data set	Real	Imaginary	Final	Detector	Null	Hot
LHSS	1.77	2.58	2.20	1.75	1.39	2.40
LHSF	2.24	2.34	2.37	2.20	1.10	2.93
LLSS	1.53	2.20	1.96	1.49	1.34	1.79
LLSF	1.30	1.66	1.52	1.25	1.29	1.21
LLLF	1.13	1.11	1.13	1.10	1.14	1.05
RHSS	2.10	3.44	2.79	2.08	1.12	3.90
RHSF	2.28	2.42	2.40	2.24	1.06	3.05
RLSS	1.46	1.34	1.53	1.41	1.40	1.44
RLSF	1.18	1.15	1.20	1.14	1.11	1.16
RLLF	1.13	1.12	1.15	1.10	1.10	1.10

---

See text for details.

In all of the data sets a few coadds still have high  $\chi^2$  and these are removed from the data. The reason for the high  $\chi^2$  was understood for some of these but for others no apparent reason was found. There were more of them at high temperatures but some were found in the low temperature null data as well. Less than 10% of the data were eliminated in this way.

## 5.6. Application of Calibration Models

The application of the calibration models to the sky data is summarized here and is described in detail in Appendix C. The input interferogram is defined as a function of optical path difference by the equation:

$$I(x) = \int_{-\infty}^{+\infty} d\nu Z(\omega)B(\omega) \sum_{i=1}^N E_i(\nu)S_i(\nu) \cos(2\pi\nu x) \quad (11)$$

where  $x$  is the optical path difference,  $\nu$  is the optical frequency in  $\text{cm}^{-1}$ ,  $\omega$  is the audio frequency in  $\text{rad/s}$ ,  $Z(\omega)$  is the electronics transfer function,  $B(\omega)$  is the bolometer response function, (see equation 9) and the sum over  $i$  represents the contribution from  $N$  sources with emissivity  $E_i(\nu)$  and spectrum  $S_i(\nu)$ . The  $N$  inputs are the sky or external calibrator and various instrument components (primarily the internal calibrator).

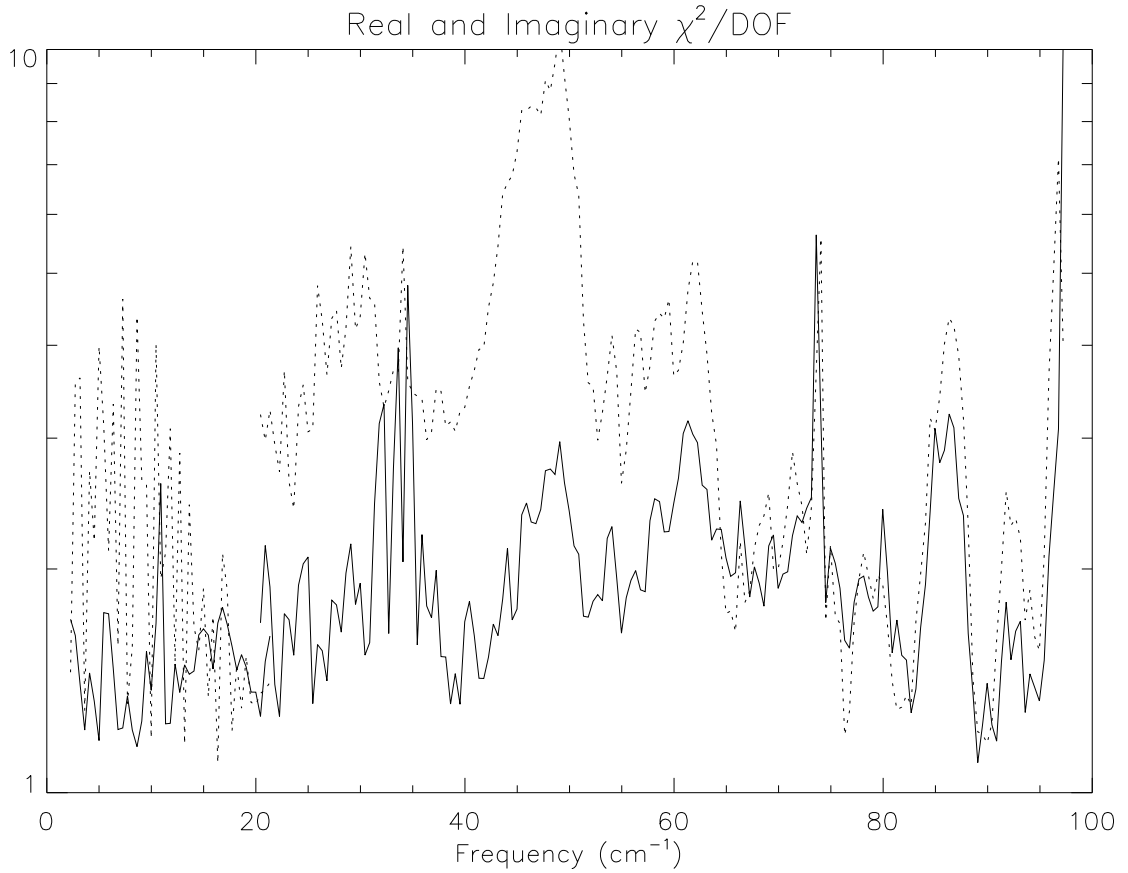


Fig. 5.4.—  $\chi^2/\text{DOF}$  as a function of frequency — The values for the real part of the spectrum (solid line) and the imaginary part (dotted line) for LLSS ( $\nu < 22$ ) and RHSS ( $\nu > 21$ ) are plotted. Note vibration lines at 10.6 and 73.5, and bands at  $73.5 - 2 \cdot 10.6 = 52.3$ ,  $73.5 - 10.6 = 62.9$ ,  $73.5 + 10.6 = 84.1$  and  $73.5 + 2 \cdot 10.6 = 94.7$ . The three-spike feature from 30 to 35  $\text{cm}^{-1}$  is a robust artifact from an unknown source.

---

A coadded IFG is apodized and Fourier transformed into a spectrum in counts:

$$Y(\nu) = \int_{-\infty}^{+\infty} A(x) I(x) e^{2\pi i \nu x} dx = a(\nu) * \left( Z(\omega) B(\omega) \sum_{i=1}^N E_i(\nu) S_i(\nu) \right) \quad (12)$$

where  $*$  is the convolution operator,  $A(x)$  is the apodization function discussed in Section 5.1, and  $a(\nu)$  is the Fourier transform of the apodization function including padding.

The spectrum in counts is normalized by the electronics transfer function to yield a spectrum in volts. The bolometer response function is computed for the spectrum based on its commanded bias, readout voltage, and bolometer temperature. The bolometer response function and the optical transfer function  $H(\nu)$  (from the XCAL emission) are used to convert the spectrum from volts to MJy/sr, yielding a differential calibrated spectrum of the sky or XCAL (a spectrum of the difference in signal between the sky or XCAL and the ICAL):

$$D(\nu) = e^{i\nu\psi} H(\nu)^{-1} \left( \frac{1}{Z(\omega)B(\omega)} Y(\nu) - C(\nu) \right) \quad (13)$$

The vibration and harmonic corrections  $C(\nu)$  are then applied to the differential spectrum. There is a small phase jitter in the *FIRAS* data which is corrected in each differential spectrum by the application of a linear autophase correction  $\psi$  which is computed to minimize the imaginary part of the spectrum.

The instrument emissivities are used to compute a spectrum of the internal calibrator using Planck functions  $P(T, \nu)$  of the measured temperatures of the instrument components for the source spectra:

$$R(\nu) = H(\nu)^{-1} \sum_{i=1}^{N-1} E_i(\nu) P(T_i, \nu) \quad (14)$$

where  $N - 1$  signifies that the source is not included in the spectrum.

The differential spectrum and the internal calibrator spectrum are combined to produce a calibrated spectrum of the sky:

$$S_{sky}(\nu) = e^{i\nu\psi} H(\nu)^{-1} \left( \frac{Y(\nu)}{Z(\omega)B(\omega)} - C(\nu) \right) - H(\nu)^{-1} \sum_{i=1}^{N-1} E_i(\nu) P(T_i, \nu) \quad (15)$$

The calibration models are applied to the calibration data using this algorithm to provide the zero-point reference for the post-calibration destriper processing described in Section 6. The sky data are similarly calibrated, and are then Doppler-shifted from the spacecraft

frame-of-reference to the solar system barycentric frame-of-reference. The number of spectra in each calibration data set is given in Table 5.3 while the number of spectra in each sky data set is given in Table 5.4.

The project data release includes: the ten calibration models; the time-ordered calibrated and differential calibration spectra for each of the 14 individual channels; and the pixel-ordered calibrated and differential sky spectra for each of the 14 individual channels. The FITS headers for all of these data sets, which are given in Appendix G, include the names and descriptions of each of the data fields.

Table 5.3: Number of Spectra in *FIRAS* Calibration Data

	LHSS	LHSF	LHLF	RHSS	RHSF	RHLF		
Spectra	512	70	177	510	71	177		
Spectra Used	495	58	176	482	55	176		
IFGs	24485	2186	7161	24647	2199	7398		
	LLSS	LLFS	LLFL	LLLF	RLSS	RLFS	RLFL	RLLF
Spectra	512	69	170	170	515	71	174	174
Spectra Used	418	28	138	140	423	34	140	142
IFGs	24300	2146	6410	6410	24456	2267	7084	7084

Table 5.4: Number of Spectra in *FIRAS* Skymaps

	LHSS	LHSF	LHLF	RHSS	RHSF	RHLF		
Pixels	5967	2092	5962	5972	2089	5954		
Spectra	35284	5099	28183	34957	5086	28185		
IFGs	130857	36846	133149	130102	36982	134183		
	LLSS	LLFS	LLFL	LLLF	RLSS	RLFS	RLFL	RLLF
Pixels	5970	2090	5956	5956	5976	2089	5952	5952
Spectra	34819	5048	27313	27313	34881	5140	27697	27697
IFGs	127098	35989	121406	121406	127047	36931	122924	122924